LJMU Research Online

Zhang, G, Lee, C, Harvey, DM, Ma, HW and Braden, D

 Finite Element Modelling for the Investigation of Edge Effect in Acoustic Micro Imaging of Microelectronic Packages

http://researchonline.ljmu.ac.uk/id/eprint/3465/

Article

For more information please contact researchonline@ljmu.ac.uk

Finite Element Modelling for the Investigation of Edge Effect in Acoustic Micro Imaging of Microelectronic Packages

Chean Shen Lee[1], Guang-Ming Zhang[1], David M Harvey[1], Hong-Wei Ma[2], Derek R. Braden[3]*

[1]*General Engineering Research Institute, Liverpool John Moores University, Byrom Street, Liverpool, L3 3AF, United Kingdom*

[2]*School of Mechanical Engineering, Xi'an University of Science and Technology, Xi'an, 710054, China*

[3]*Delphi Electronics and Safety, Kirkby, Liverpool, UK*

[*] Corresponding author. Tel: +44-1512312113; E-mail: g.zhang@ljmu.ac.uk.

Abstract

In acoustic micro imaging of microelectronic packages, edge effect is often presented as artifacts of C-scan images, which may potentially obscure the detection of defects such as cracks and voids in the solder joints. The cause of edge effect is debatable. In this paper, a two-dimensional finite element model is developed on the basis of acoustic micro imaging of a flip-chip package using a 230 MHz focused transducer to investigate acoustic propagation inside the package in attempt to elucidate the fundamental mechanism that causes the edge effect. A virtual transducer is designed in the finite element model to reduce the coupling fluid domain, and its performance is characterised against the physical transducer specification. The numerical results showed that the Under Bump Metallization (UBM) structure inside the package has a significant impact on the edge effect. Simulated wavefields also showed that the edge effect is mainly attributed to the horizontal scatter, which is observed in the interface of silicon die-to-the outer radius of solder bump. The horizontal scatter occurs even for a flip-chip package without the UBM structure.

Keywords: Acoustic simulation; Acoustic micro imaging; Microelectronic packages; Edge effect; Horizontal scatter

1   Introduction

Microelectronic packages are required to accommodate increasing numbers of I/O channels while shrinking in overall size forcing tighter and finer pitches. In addition to miniaturization, modern microelectronic packages include multiple stacked dies which heterogeneously integrates multiple electronic modules. Even with careful manufacturing, delamination in between material interfaces, discontinuities in the electrical connections, cracked dies, voids in the under fill and introduction of air gaps are common. The increasing complexities of microelectronic packages bring a big challenge to microelectronic reliability.

Acoustic micro imaging (AMI) (also known as Scanning Acoustic Microscopy) is a very important non-destructive evaluation tool for failure analysis and reliability testing of modern microelectronic packages. Acoustic micro imaging relies on the acoustic impedance differences of various material interfaces, and is particularly sensitive to gap type defects such as voids, cracks and delaminations as small as ~0.1 μm [1]. A focused transducer emits an acoustic pulse into the test sample and receives the reflected echoes while mechanically scanning the transducer across the sample. Acoustic images are largely presented in three basic formats: an A-scan is an acoustic signal received at an X-Y position, consisting of reflected echoes from multiple interfaces as the acoustic pulse travels deep into the sample; a B-scan represents a cross-sectional image as the transducer scans in a lateral axis; a C-scan is obtained when the plane of the sample is mechanically scanned with the transducer focused and gated on a specific interface/depth. Samples are usually submerged in water to improve coupling between the ultrasonic transducer and the test sample. For microelectronic packages, typical transducer frequencies range from 50 MHz to 500 MHz, where higher frequencies translate into better resolution but with less penetration.

Figure 1 shows a C-scan image acquired using a 230MHz transducer, of the silicon die-to-solder bump interface produced from the detection of a flip-chip package soldered on a PCB board. The test sample and experimental details can be found in [1,2]. Edge Effect [1, 2] is

commonly observed in acoustic micro imaging of microelectronic packages. The phenomenon is usually observed at the edge or perimeter of the die or package as well as on the outer radius of solder bumps as shown in Figure 1a. Especially for solder joints, the phenomenon manifests itself as a dark ring around the solder bump as shown in Figure 1b, indicating that most if not all of the incident acoustic energy has been 'scattered' by the curvature of the solder bump geometry. The dark annular region obscures the detection of defects such as cracks and voids inside the solder bump. Detection of defects at the periphery of joints is particularly difficult due to the edge effect. Consequently, the interpretation of C-scan images and defect detection of solder joints is very difficult. Notice that in an actual C-scan image, edge effect in some solder joints may not be always a complete ring. This is due to various reasons, such as that the top surface of the flip-chip package is not placed strictly level when acquiring the C-scan image, the solder paste is not applied evenly when fabricating the package, and the solder joints are placed very close to the die perimeter.

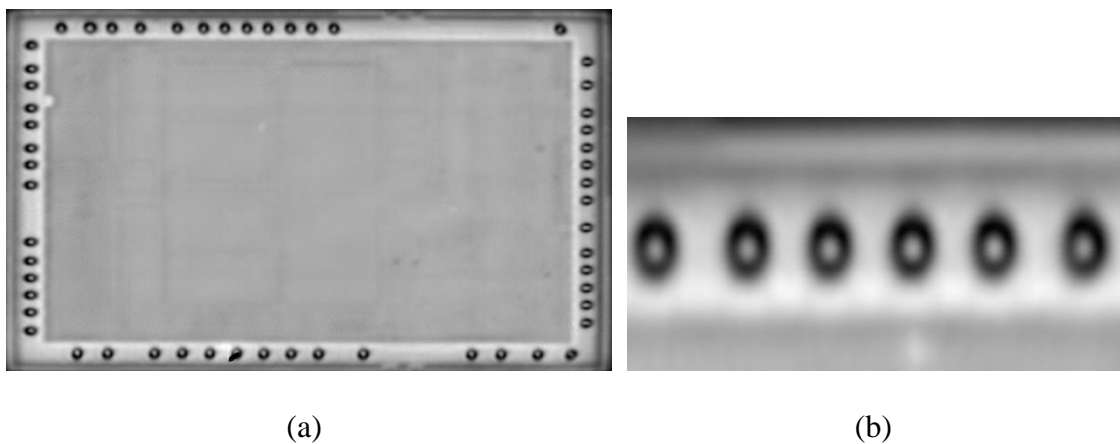(a)   (b)

Figure 1: (a) A C-scan image of die-solder bump interface obtained from detection of a flip-chip package soldered on a PCB board using a 230MHz transducer; (b) Magnified view of solder joints from Figure 1a.

It is widely accepted that the edge effect occurs when the acoustic wave is 'scattered' either by the edge geometry or refracted when the ultrasonic pulse is propagating through various materials [3]. The physical explanation for the edge effect generation is debatable. Moreover, the acoustic propagation within the solid specimen cannot be measured directly. In our earlier study, finite element modelling was proposed to investigate acoustic propagation inside microelectronic packages, and the basic finite element model and preliminary results were reported in [4]. In [5, 6], C-line plot technique was developed for characterisation of edge effects in acoustic C-scan images, in particular solder joint C-scan images. In this paper, the model is further improved by introducing the dynamic meshing, more suitable material properties, characterisation of virtual transducer, etc. Moreover, Acoustic Propagation Map (APM) is further developed to intuitively observe the interaction of acoustic waves with internal structures of the flip-chip package, and quantitative measurement of acoustic wavefields is carried out to analyse the acoustic energy loss inside the package in an attempt to elucidate the fundamental mechanism that causes the edge effect.

2   Finite Element Modelling of AMI of a Flip-Chip Package

AMI of a flip-chip package is modelled using the commercial finite element software, Ansys 12.0. A two-dimensional (2D) finite element model as shown in Figure 2 is developed on the basis of AMI of a flip-chip package using a Sonoscan 230 MHz focused transducer as used in our experiment study (Sonoscan Inc, Gen6™ C-SAM, Elk Grove Village, IL, USA) [1, 2]. The physical transducer with a lens diameter of 4750 μm, a focal length of 9500 μm, a spot size of 16 μm, and a focal depth (depth of focus) of 186 μm in water, is commonly used in AMI of microelectronic packages. The silicon die of the flip-chip package has a thickness of 725 μm, and the diameter of a solder bump is 140 μm. The solder bump material is Tin-Lead (60:40). The silicon die and solder bump are soldered together through a thin Under Bump Metallization (UBM) structure. UBM with a thickness of 10 μm is modelled by a

representative sandwich structure consisting of Al, NiV, and Cu layers at ratio 1:1:1. The material properties used in the model are presented in Table 1.
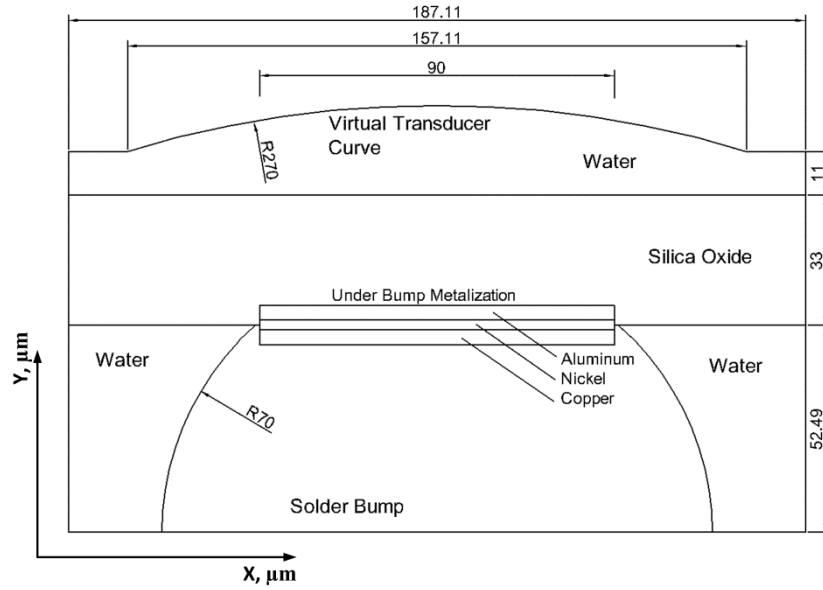

Figure 2: The geometrical model for AMI of a flip-chip package (unit in μm).

Table 1: Material properties used in the finite element modelling

Material	Density (kg/m^3)	Acoustic Velocity (m/s)	Young's Modulus (GPa)	Poisson Ratio	Source
Water	1000	1484			[7]
Die Wafer Silica (110 Orientation)	2330	7695	138	0.361	[8]
Eutectic Tin-Lead Solder (60:40)	8420	2159	38.6	0.36	[9]
Aluminum 2024-T3	2780	5000	69.5	0.28	[10]
Electronic Grade Copper (C101)	8920	3773	127	0.345	[8]
Pure Nickel	8890	4860	210	0.31	[11]

Microscale simulations of AMI of microelectronic packages with ultrasound frequencies in the hundred megahertz range require a high computational cost since the element density is tied to the wavelength. Moreover, in reliability testing of flip-chip packages, the die-to-solder bump interface is the most interested area since the solder joints are particularly vulnerable to crack initiations at the die-to-solder bump interface [12]. In order to focus on this interface, the transducer has to be placed several millimetres above the surface of the flip-chip package. Such a scale will present a problem for a high-frequency acoustic simulation. Modelling the physical transducer and the actual size of the sample as well as the coupling water zone in a personal computer is impractical due to the huge computational resources requirement. To put this into perspective, at 15 elements per wavelength as recommended by [13] (20 is recommended in [12, 14] that would pose even greater execution times), the coupling medium alone requires 180 million elements. Without distributed computing, independent terminals can manage a range of 100-200 thousand elements, which would take a period of days to be solved over using shared-memory on multi-core processors.

Three ways are developed to reduce the elements in our modelling. Firstly, subsections and dynamic meshing are used. This practise involves concentrating the element densities around the area of interests so save cost as shown in [15-17]. Details are presented in Section 2.1. Secondly, a virtual transducer is designed to replace the physical transducer, as a result reducing the transducer size and the coupling water zone. Details are presented in Section 2.2. Thirdly, the thickness of the silicon die is reduced since our interest is the die-to-solder bump interface. A silicon die thickness of $33\,\mu$m was specified in the finite element model to calibrate the focal point of the virtual transducer into the middle of the UBM structure. Through the three ways, the processing time of the solution in our personal computer (Intel Core i7) is reduced to within 100 hours.

In the 2D finite element model shown in Figure 2, the transducer only scans along the x-axis. The y-axis in the 2D model is the depth direction. When scanning the transducer, at

each transducer position requires a reiteration of the finite element solution. Each iteration produces one A-scan. For brevity, each solution and its corresponding transducer position will be referred as iteration-X µm where X is the centre position of the virtual transducer (VT). Iteration-0 µm is the solution where the centre of the VT is coincident with the centre of the solder bump. At iteration-70 µm, the VT position is at the edge of the solder bump when the central axis is tangential to the edge of the solder bump. To be comprehensive, the model is solved up to iteration-80 µm. Figure 3 shows the finite element model at the initial and final iteration in this study. The scanning resolution for this study is set as 1 µm. It can be arbitrarily adjusted with a linear impact on the computational cost. The model shown in Figure 2 is solved with (Model A) and without (Model B) the UBM structure. The data is organized into two sets with 80 iterations each.
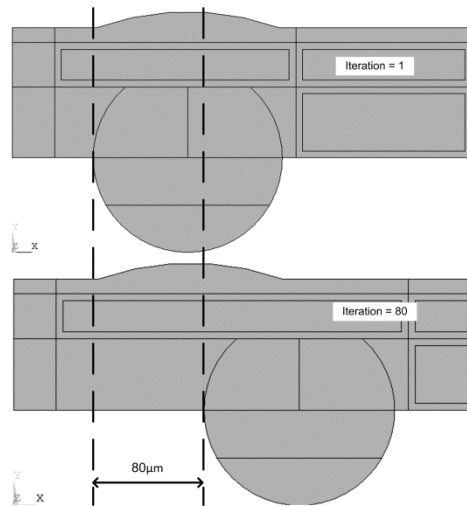

Figure 3: The position of the solder bump is offset to emulate the transducer mechanical scanning in acoustic micro imaging.

In order to investigate the acoustic propagation inside the microelectronic packages, a post-processing algorithm, Acoustic Propagation Map, is developed to present transient acoustic data in a single image. This is achieved by compressing a series of transient acoustic wavefields obtained during the wave propagation across the time domain into one acoustic

wavefield image. APM gives a good summary of the transducer beam profile inside the solid showing scatters, refractions, reflections and transmissions, and allows measurements of isolated regions in the APM image to obtain quantitative data. Figure 4 illustrates the merging process. The solution from every time step of the simulation is inserted into a three dimensional array as a page. Each page of the matrix represents an acoustic wavefield in a transient time step, which contains displacement and pressure data (respectively for solid and fluid regions). To study these acoustic data types as a unit of energy, the acoustic data is squared to obtain the "intensity" of the displacement and pressure. Fixing the column and row for each pixel, e.g. A, B and C in Figure 4, the data is Sum or Max along the page dimension. Each operation provides a different aspect of evaluation: Summation will add all the acoustic energy experienced at each point, revealing information on reflections and vector; Maximum will plot the path of the strongest acoustic energy, isolating direction and magnitude of specific waves.
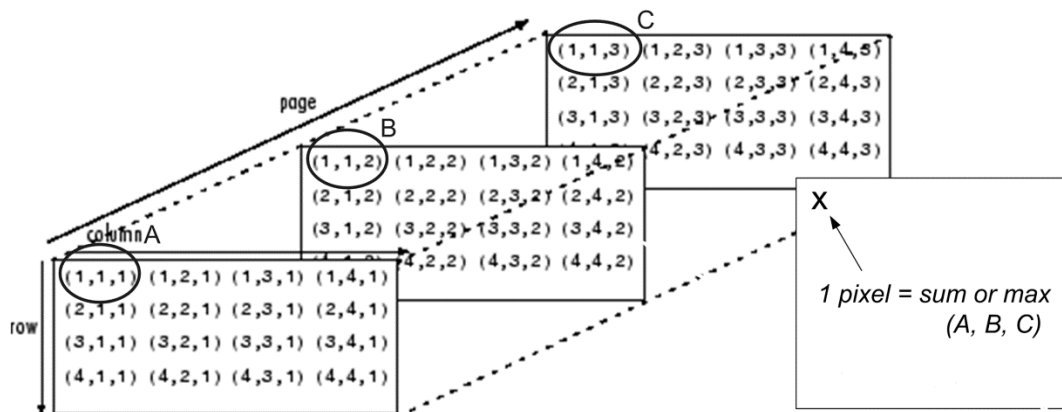

Figure 4: Creation of an APM image by compressing acoustic wavefields at a series of transient time steps.

2.1 Finite elements and boundary conditions

Three types of finite elements are used in this finite element modelling. FLUID29 represents the liquid medium, PLANE42 is used to model the solid flip-chip package, and a truncated absorbing boundary is created using a mixture of FLUID129 infinite boundary and FLUID29 Perfectly Matched Layers (PML) to suppress the computational artefacts. The truncated boundary is necessary because it is unrealistic to model an infinitely big buffer domain. The solder bump, silicon die and UBM are modelled using PLANE42 solid elements. Figure 5a shows the area segments used to define and aid the dynamic mesh creation process. Areas A1, A12, A13, A22 and A23 (A22 overlaps with A23) define the silicon region. While A18, A5, A8 and A4 models the solder bump. The thin layers in between the silicon and solder bump are the UBM, which has 4 layers in the model instead of 3, the centre twin layers are defined with the same material properties.

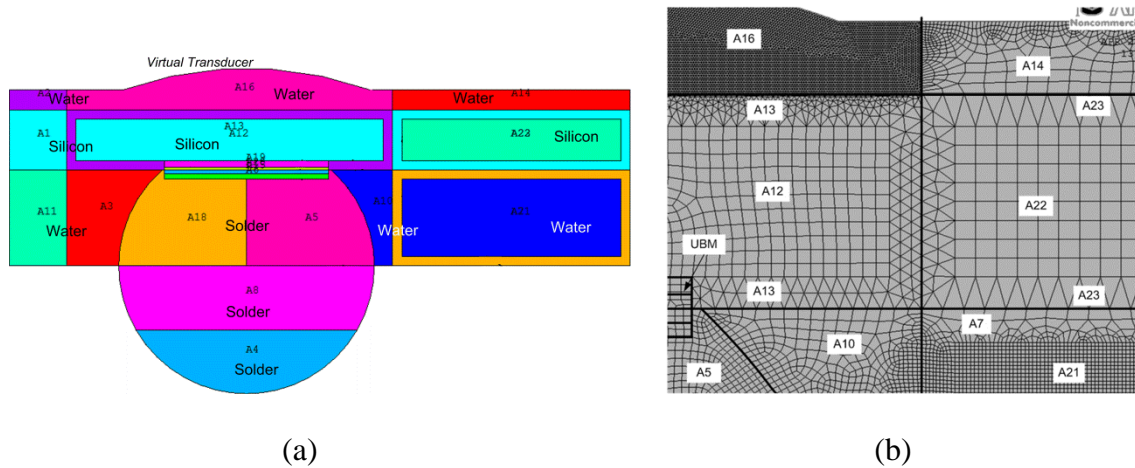|	
(a)	(b)

Figure 5: (a) Area segments in the proposed finite element model; (b) Dynamic meshing.

At each *iteration*, the solder bump position is shifted to model the mechanical scanning used in a real AMI system. Since the scanning point begins at the centre of the solder bump and shifts to the outer edges, the model is not divisible by half. This makes the model asymmetrical since the whole solder bump is modelled and any kind of mirroring will

introduce another copy the sample during the scanning process. Therefore, this model does not benefit from symmetrical half modelling. Fortunately, the resultant B-Scan data is symmetrical, hence the transducer scanning only needs to cover half the solder bump. The buffer zones provided by column group A14, to A21 allows the solder bump to manoeuvre horizontally without clipping the model.

Since the element density for acoustic simulation depends largely on the acoustic wavelength in the respective material, different mesh densities of area segments across the model are used as illustrated in Figure 5b. The boundary between segments with mismatched density changes are modelled with a 'frame' of several elements thick to allow smooth transitions between densities. This is demonstrated in A12 and A22 with their respective frames A13 and A23. The frame uses triangular elements which are well suited for mapping odd geometries and is very robust when matching element density changes. Without the frame, the automatic element creation algorithm will result in a highly distorted element map as seen in A14. In this case, A14 is a buffer zone and therefore element imperfections can be ignored.
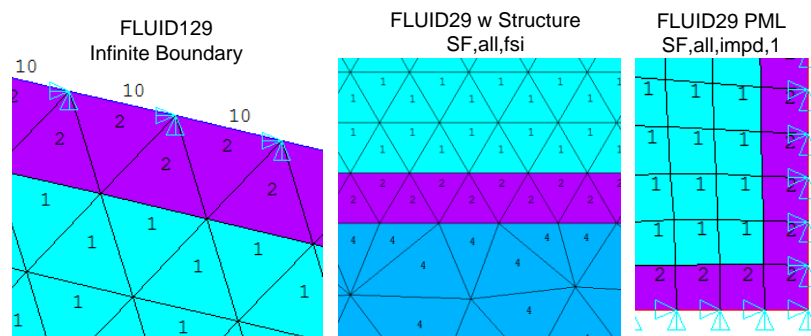

Figure 6: Absorbing and interfaced boundary conditions.

As illustrated in Figure 6, there are three boundary conditions implemented. The virtual transducer curve is fitted with element type 10, which is the arbitrary designation for

FLUID129 infinite boundary. Virtually all interface interactions require that the fluid-structure interface flag for FLUID29 to be activated, as indicated by the presence of element type 2. Element type 1 is lossless non-structural FLUID29 element which only has pressure degree of freedom. The pressure data is translated into displacements at the interface between element 2 and 4 with 'SF, all, FSI' flag activated. These displacement data are asymptotically expanded into infinity when interfacing with FLUID129, or numerically suppressed (PML) at the computational boundaries when 'SF, all, IMPD,1' is activated. The arrows in Figure 6 indicate constrained displacement degree of freedom which is applied to the entire boundary.

2.2   Virtual transducer and characterization

In order to reduce the computational load, the physical transducer is scaled down to microscale in the finite elemental model as shown in Figure 7. A VT is mathematically derived by vectoring the wave displacements to match the characteristics of an ideal acoustic wave at a specific time and space. This emulates ideal uninterrupted ultrasonic pulse propagation in the fluid medium and significantly reduces computational cost and wastage. To construct the VT, there are two key parameters: the curvature of the VT and the length of the arc. The length of arc as shown in Figure 7 defines the active region of the VT geometry which is coupled with pressure loads and data points to transmit and receive acoustic signals. The arc length is related to the chord length of the circle given as:

$$Chord = 2R \sin(\arcsin \frac{C_0}{2R_0}), \qquad (1)$$

where R is the radius of the VT curve, C_0 and R_0 are the lens diameter and focal length of the physical transducer respectively. This allows a transducer to be modelled very close to the sample. The virtual transducer was constructed against the Sonoscan 230MHz transducer used in our experimental study.
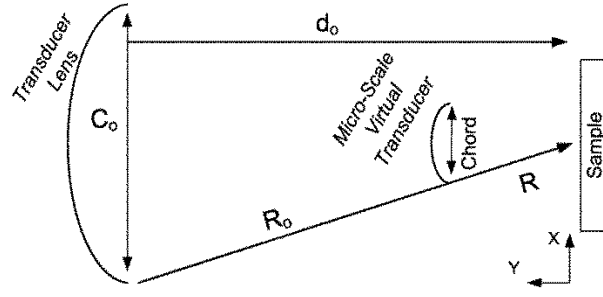
Figure 7: The construction principle of a virtual transducer.

The ultrasonic signal is usually a broadband pulse modulated at the centre frequency of the transducer, and is usually modelled as a Gabor function as follows:

$$f(t) = A \cdot \exp\left(-\frac{\pi(t-u)^2}{\sigma^2}\right) \cdot \cos(\omega(t-u)), \qquad (2)$$

where A is the reference amplitude, ω is the frequency modulation and u its translation and σ controls the envelope of the Gaussian function. In order to examine the efficiency of the Gabor model for approximating ultrasonic pulses in our system, ultrasonic echoes reflected from the front surface of a steel block in a water tank were collected using the 230 MHz focused transducer in our previous study [18]. The measured echoes were then fitted by the cosine Gabor model. The root-mean squared error of disparity between the estimated and measured echoes is 1.12%. Thus, the input load applied to the virtual transducer was modulated using the Gabor function in Equation (2). The parameters in Equation (2) were obtained by approximating the measured ultrasonic echo using the Gabor model. The parameters specifically for the physical 230 MHz transducer used are $\omega = 0.4396$ and $\sigma = 19.1943$. The acoustic loads are then vectored at a tangent to the virtual transducer curve. The length of excitation load along the virtual transducer is dependent on the chord as shown in

Figure 7 and Equation (1). In this paper, the chord has a length of 98.74 μm and a curvature radius of 199.2 μm.

To characterize the designed virtual transducer, a transient simulation was carried out in a water medium. The beam profile of the virtual transducer created using APM with the sum operation is shown in Figure 8a. Figures 8b and 8c show the max amplitude profiles along the two lines labelled in Figure 8a. The focal depth of the virtual transducer is then measured as 192 μm from Figure 8b, and the spot size is measured as 15 μm from Figure 8c. Compared to the physical transducer, the virtual transducer has a deviation of 3.1% for the focal depth and 6.2% for the spot size. Furthermore, in order to verify the frequency domain characterisation of the virtual transducer, Fast Fourier Transform was applied to the acoustic pulses, and the centre frequency and bandwidth of the virtual transducer are measured as 235.2 MHz and 100 MHz respectively, which are very close to the characteristics of the physical transducer.
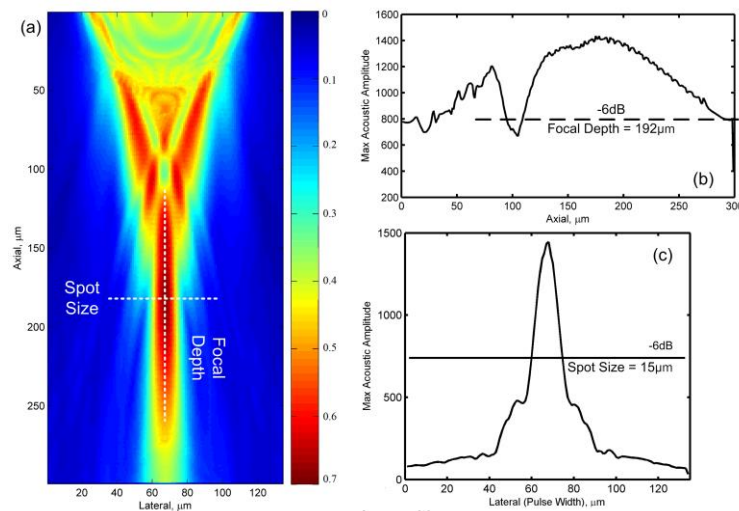

Figure 8: (a) Beam profile of the virtual transducer with focal depth and spot size measurements shown as (b) and (c) against the physical transducer with a spot size of 16 μm and a focal depth of 186 μm.

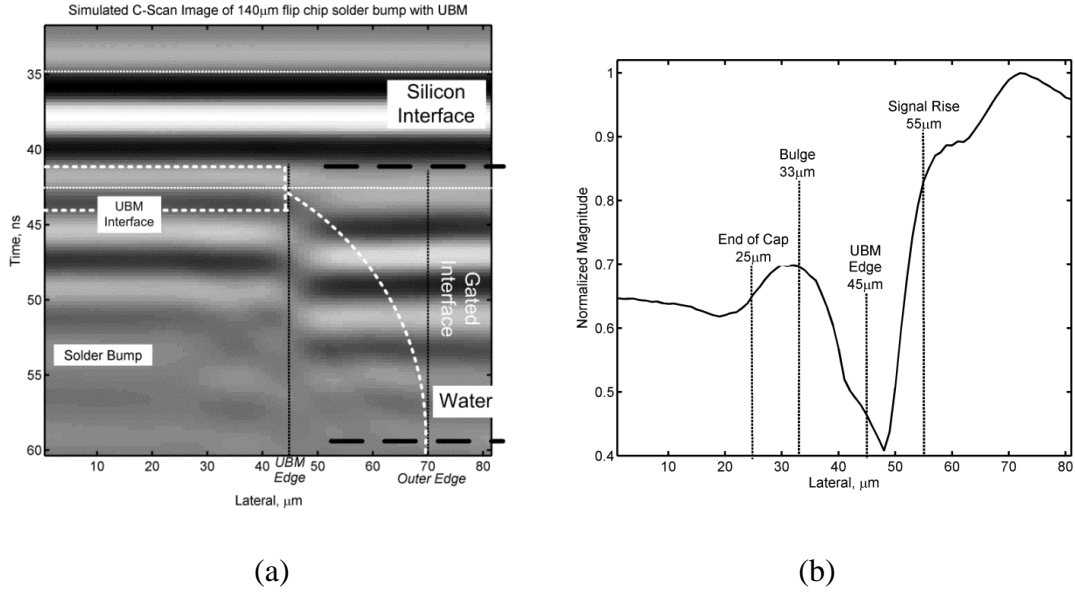## 2.3   Simulation of AMI of the flip-chip package and edge effect

Figure 9: (a) A simulated B-scan for the flip-chip package using the finite element modelling shown in Figure 2; (b) The resulting C-Line plot.

Figure 9a shows the obtained B-scan image using Model A. In order to study edge effect, a C-Line plot [4, 5] as shown in Figure 9b is generated by gating the B-scan image to the desired interface, similar to real C-scan imaging. Since we are interested in the silicon die-to-solder bump interface, the gate is set to select that interface. The C-line plot is equivalent to a cross-sectional profile of the C-scan images shown in Figure 1. As the transducer moves towards the edge of the solder bump at $70\,\mu m$, the image intensity increases due to high reflection from the silicon die-to-water interface. Overall, this creates a 'valley' profile which characterizes the edge effect.

3   Investigation of Edge Effect in Acoustic Micro Imaging of the Flip-Chip Package
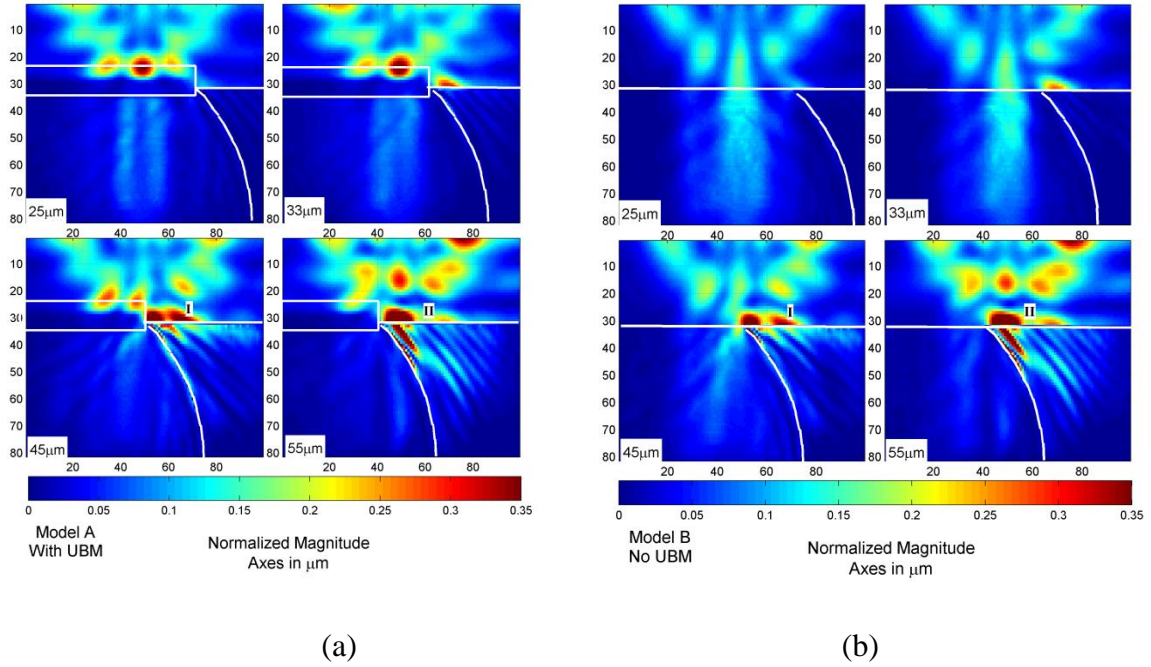
Figure 10: APMs obtained using the sum operation at four transducer positions for (a) Model A and (b) Model B.

Figure 10 shows the acoustic propagation maps obtained by the sum operation from the model A and model B respectively. In all the images, the displacement magnitude data (for solid) is merged with the pressure magnitude data (for fluid) to produce a complete map. Notice that each image is normalized against the largest value from the entire data set throughout the paper, therefore uniting the image scale.

The APM in Figure 10a shows the 'scattered' acoustic energy in the fluid region increasing as the VT is positioned closer to the solder bump edge. This preliminary observation is in line with the popular assumption that the edge effect is generated mainly from acoustic energy 'scattered' by the solder joint edges.

Figure 10 shows significant magnitude at the silicon-to-water interface in iteration 45 μm and 55 μm at points (i) and (ii) indicated in the figure. This indicates strong reflection as the incident and reflected waves are added together by the sum operation. This clearly indicates a strong reflection due to the high impedance mismatch between silicon and water.

From Figure 10, it is observed that the contour profile of (i) and (ii) are very similar in both Model A and Model B. At the transducer position of 45 μm, the edge effect occurs while the C-Line has higher magnitudes at 55 μm. This effect is most likely caused by specific interactions with the UBM structure.

From Figure 10a at iteration = 45 μm, while the edge effect is apparent, a small amount of acoustic energy is observed within the solder bump. Defect detection may still be possible under these circumstances. However, at iteration 55 μm the acoustic propagation maps of both the Models A and B show only tiny quantities of acoustic energy propagated into the solder bump. This will hinder the detection of any defects inside the solder bump.

From Figures 10, it is observed that the acoustic energy is focused on the UBM through a complex mode of propagation. The bulk of the acoustic energy is not propagating through the centre of the focal axis as one might expect. Instead the propagation mode channels, the bulk of the acoustic energy along the outer edges of the focal beam also shows a predictably strong reflection from the silicon-to-water interface.

Without the UBM in Figure 10b, a significant amount of acoustic energy is able to propagate into the solder bump. This immediately shows that the UBM structure has a considerable effect on acoustic penetration despite being very thin. This is due to the impedance mismatch and its multi-layered structure. At iterations 45 μm and 55 μm, the acoustic energy available in the solder bump is still largely blocked by the edge. This also immediately shows that defect detection in the solder bump cannot easily occur at regions without a physical connection directly above it.

3.1   *Analysis of acoustic energy loss*

From Figures 9 and 10, it can be seen that the edge effect C-Line profile has a relationship with the acoustic energy loss in this region. This section tracks the acoustic energy loss in the presence of edge effect during AMI of the flip-chip packages. At the die-to-solder bump

interface, the acoustic energy may be lost through the solder bump edge 'scattering', refraction, and mode conversion. Figure 11 shows a magnified view of the acoustic propagation maps from the iteration 45 µm using the max operation for both Model A and Model B. The APM shows similar propagation profiles of 'scattered' acoustic energy in the fluid region for both Model A and Model B. Two marginal differences can be observed. First, in the grid marked by α, the dark blue contour shows the UBM reflecting significant amounts of the acoustic energy and preventing penetration into the solder bump. The grid marked by β shows that the 'scattering' from the UBM edge has increased the amount of acoustic energy interfacing with the solder bump edge, causing a marginal increase in 'scattered' energy.
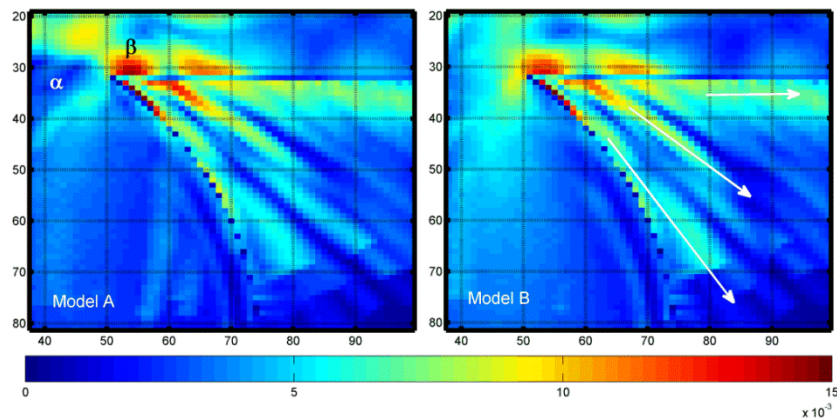

Figure 11: Magnified view of APMs obtained using the max operation for Models A and B at iteration 45 µm.

The maps generated using the max operation will only map the largest pressure experienced at any pixel during the entire 60ns duration. This will provide an intuitive visualization of the propagation paths of acoustic energy which are 'scattered' into the fluid. As indicated by the arrows in Figure 11, the 'scattered' acoustic energy attenuates rapidly in the fluid medium. The bands are caused by the superposition of waves originating from various sources. The bands also show the general direction of the vector sum. It can be seen

that the acoustic energy is scattered in a generally diagonal path. Direct tracking of these waves is unattainable in the current simulation configuration. From a theoretical basis, these sources may include a combination of: 1) Refraction from the silicon plane and solder bump; 2) Scattering from the edge of the solder bump; 3) Leaked Lamb waves occuring due to the mode conversion in the die-to-solder bump interface as the thickness of the silicon die is comparable to the ultrasonic wavelength.

Both models in Figure 11 show a solid band along the silicon die marked by the horizontal arrow. This unbroken trail on the acoustic maps shows a considerable amount of acoustic energy scattered in a horizontal vector (abbreviated as horizontal scatter). The lack of interference pattern also indicates a solid pulse of energy travelling in that vector. The data suggests that a large portion of the scattered waves are refracted close to the horizontal vector when the centre of acoustic pulse interfaces the die-to-solder bump edge. This may explain some of the loss of acoustic energy which generates the edge effect. The data also show that the horizontal scatter is not affected by the presence of the UBM since it is present in both Models A and B and is caused primarily by the 'silicon die-solder bump' edge.

The horizontal 'scatter' is illustrated further by comparing the acoustic propagation maps obtained when the transducer is located at 45 μm and 55 μm as shown in Figure 12. The mechanism of horizontal scatter is only observed when the transducer is moving to the positions where the edge effect occurs. This is important since any y-axis propagation will be reflected, while all energy on the horizontal scatter cannot be received by the transducer. This suggests that the horizontal scatter is a significant factor in edge effect generation.
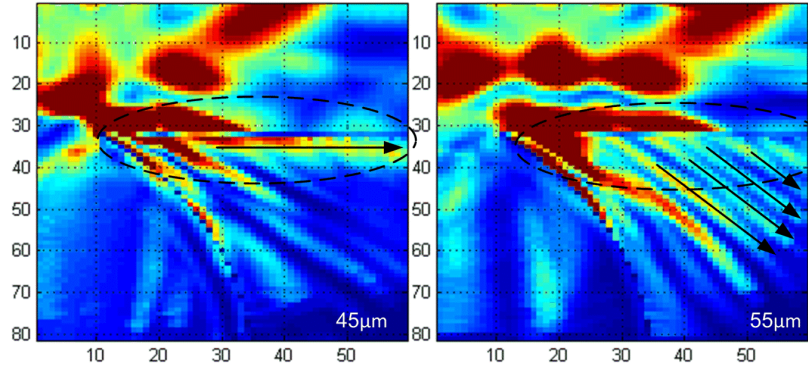
Figure 12: Magnified view of APMs for Model A at iterations 45 µm and 55 µm using the max operation.

3.2 Analysis of energy in solder bump region

In order to understand the impact of the UBM presence on acoustic penetration, in this section we measure the difference in acoustic energy present in the solder bump with and without the UBM. Quantifying the amount of acoustic energy present in the solder bump past the UBM structure will have beneficial implications for future design work. It also provides a general guidance to help assess the maximum possible intensity of the reflected echo by void type defects within the solder bump.
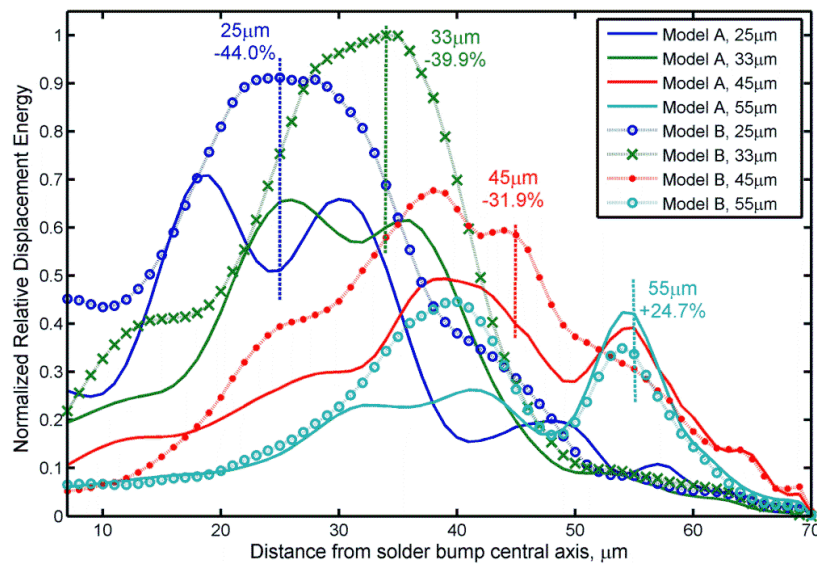
Figure 13: Total acoustic energy penetrating into the solder bump between Models A and B at four transducer positions.

Figure 13 presented the total acoustic energy for Models A and B at four transducer positions. Between iterations $25\,\mu m$ to $45\,\mu m$, the acoustic energy in Model A are between 44% to 31.9%, which are lower than the corresponding Model B results. However at iteration $55\,\mu m$, the acoustic energy inside the solder bump is actually higher in Model A than Model B. The explanation needs further study. The plots in Figure 13 show the maximum amount of acoustic energy possible in such a structure as well as the amount of energy lost by the UBM.

4   Discussions

There are many other approaches to model acoustic wavefields, such as hybrid FEM/analytical approaches or perhaps more analytical approaches that are generally well-developed for bulk wave NDE. In this paper, we choose FEM because it facilitates us to the interaction of acoustic wave with internal structures and to do a quantitative analysis.

It is a widely held view that a temporal and spatial resolution of 20 elements and time steps per wavelength are required to suppress numerical dispersion errors. However, the spatial resolution had a quadratic increase to computational cost while temporal resolution had a linear cost increase. An elaborate study to evaluate the numerical dispersion error can be found in [6]. It concluded that: 20 elements per wavelength has a correlation 0.99 to the control result;15 elements per wavelength has a correlation of 0.95; There was no significant increase in fidelity beyond 20 elements per wavelength; 15 elements per wavelength is significantly cheaper to run; Temporal resolution of 15 is acceptable and 20 are recommended.

The causes for the bulge observed in Figure 9b, is not clear. The critical incidence angle is explored in attempt to explain the bulge, but could not confirm the source of this

phenomenon [6]. Using the point VT data to restrict the aperture of the receiving virtual transducer, it was observed that the source of the bulge originated very close to the UBM edge [6].

There is a possibility the horizontal scatter is manifested through leaky Lamb waves or surface acoustic waves since the acoustic wavelength of the silicon die at 230MHz is comparable to the die thickness. Further study is needed in the future to determine if the mode conversion is present.

From Figure 2, it can be seen that the flip-chip package is a multilayered-structure with very thin layers, especially the UBM structure. Multiple reflections among these layers exisit, leading to echo overlapping or even standing wave formation that could be another potential source of blurring of B- and C-scan images, thus contributing to the edge effect. This souce will be studied in the future by recording the acoustic date in a much smaller time step during the simulation.

5   Conclusions

A finite element model has been developed to investigate the edge effect in acoustic micro imaging of microelectronic packages. For microscale modelling, frequency related element densities and time step fidelity challenge the computational cost. In order to reduce the computational cost of modelling high-frequency transient acoustic imaging, a virtual transducer is designed in the finite element model, and its performance is characterised with a deviation of 3.1% for the focal depth, and 6.2% for the spot size measured against the physical counterpart.

Acoustic propagation inside a flip-chip package has been studied based on the proposed microscale modelling. The flip-chip package is modelled with and without a UBM structure inside. A post-processing algorithm called as acoustic propagation map has been developed to investigate the acoustic phenomena caused by the internal structures of the package. Edge

effect has been studied by tracking the acoustic energy propagation inside the package and the interaction with the internal structures of the packages. Results showed that the UBM structure has a significant impact on the edge effect. Numerical results also suggested that the horizontal scatter occurring in the silicon die-to-solder bump interface is a significant factor in edge effect generation.

Acknowledgement

References

1. R.S.H Yang, D. R. Braden, G-M. Zhang, and D. M. Harvey, An automated ultrasound inspection approach for solder joint assessment, Microelectronics Reliability, 52(12)(2012), pp. 2995-3001.

2. R.S.H Yang, D. R. Braden, G.-M. Zhang, and D. M. Harvey, Through lifetime monitoring of solder joints using Acoustic Micro Imaging, Soldering and Surface Mount Technology, 24(1) (2012), pp.30-37.

3. J.E. Semmens, Flip chips and acoustic micro imaging: An overview of past applications, present status, and roadmap for the future, Microelectronics Reliability, 40(8–10) (2000), pp. 1539-1543.

4. C. Lee, G.-M. Zhang, and D. M. Harvey. Analysis of solder joint edge effect in acoustic micro imaging of microelectronic packages: a preliminary study. in the 4th Electronic System-Integration Technology Conference (ESTC), 2012, p.1-4.

5. C. S. Lee, G-M. Zhang, D. M. Harvey, H-W Ma "Development of C-Line plot technique for the characterization of edge effects in acoustic imaging: A case study using flip chip package geometry, Microelectronics Reliability, 2015, doi:10.1016/j.microrel.2015.08.005.

6. C. Lee, Numerical study for acoustic micro-imaging of three dimensional microelectronic packages. PhD thesis, Liverpool John Moores University, 2014.

7. M. CROCKER, Handbook of Acoustics, John Wiley & Sons, 1998.

8. X. Li, G. Ding, T. ANDO, M. SHIKIDA, and K. SATO, Mechanical properties of mono-crystalline silicon thin films measured by different methods. 2006 International Symposium on Micro-NanoMechatronics and Human Science, 5-8 Nov. 2006, pp.1-6.

9. N. F. ENKE, T. J. KILINSKI, S. A. SCHROEDER, and J. R. LESNIAK, Mechanical behaviors of 60/40 tin-lead solder lap joints. IEEE Transactions on Components, Hybrids, and Manufacturing Technology, 12 (1989), pp. 459-468.

10. A. MITAVETE, Composites Design, Zaragoza, University of Zaragoza, Woodhead Publishing Limited, 1993.

11. Vic Parkville, Handbook of engineering materials, Institute of Metals and Materials Australasia, 1997.

12. R. Mohamed and P. Masson, Time Domain Spectral Element Fast Solver for Piezoelectric Structures. In International Workshop of Smart Materials, Structures and NDT in Aerospace. 2011. Canada: Canadian Institute for NDE.

13. C-H, Y. and T. Chun-Zen, Laser ultrasound measurement and finite-element simulation on the dispersion behaviors of acoustic waves propagating along wedges with bilinear cross sections, IEEE Transactions on Ultrasonics, Ferroelectrics and Frequency Control, 53(4) (2006), pp. 754-760.

14. A. L'Etang and Z. Huang, FE simulation of laser generated surface acoustic wave propagation in skin. Ultrasonics, 44(SUPPL.) (2006), pp. e1243-e1247.

15. Luis Saucedo-Mora and Thomas James Marrow, Method for the explicit insertion of microstructure in Cellular Automata Finite Element (CAFE) models based on an irregular tetrahedral Finite Element mesh: Application in a multi-scale Finite Element

Microstructure MEshfree framework (FEMME). Finite Elements in Analysis and Design, 105 (2014), pp. 56-62.

16. S.C. Li, Z.H. Xu, G.W. Ma, and W.M. Yang, An adaptive mesh refinement method for a medium with discrete fracture network: The enriched Persson's method. Finite Elements in Analysis and Design, 86(2014), pp. 41-50.

17. F. Wang and Y. Chen, Modeling study of thermosonic flip chip bonding process. Microelectronics Reliability, 52(11)(2012), pp. 2749-2755.

18. G-M. Zhang, D. M. Harvey, and D. R. Braden, Signal denoising and ultrasonic flaw detection via overcomplete and sparse representations. The Journal of the Acoustical Society of America, 124(5) (2008), pp. 2963-2972.

Table Captions

Table 1: Material properties used in the finite element modelling

Figure Captions

Figure 1: (a) A C-scan image of die-solder bump interface obtained from detection of a flip-chip package soldered on a PCB board using a 230MHz transducer; (b) Magnified view of solder joints from Figure 1a.

Figure 2: The geometrical model for AMI of a flip-chip package (unit in μm).

Figure 3: The position of the solder bump is offset to emulate the transducer mechanical scanning in acoustic micro imaging.

Figure 4: Creation of an APM image by compressing acoustic wavefields at a series of transient time steps.

Figure 5: (a) Area segments in the proposed finite element model; (b) Dynamic meshing.

Figure 6: Absorbing and interfaced boundary conditions.

Figure 7: The construction principle of a virtual transducer.

Figure 8: (a) Beam profile of the virtual transducer with focal depth and spot size measurements shown as (b) and (c) against the physical transducer with a spot size of $16\,\mu m$ and a focal depth of $186\,\mu m$.

Figure 9: (a) A simulated B-scan for the flip-chip package using the finite element modelling shown in Figure 2; (b) The resulting C-Line plot.

Figure 10: APMs obtained using the sum operation at four transducer positions for (a) Model A and (b) Model B.

Figure 11: Magnified view of APMs obtained using the max operation for Models A and B at iteration $45\,\mu m$.

Figure 12: Magnified view of APMs for Model A at iterations $45\,\mu m$ and $55\,\mu m$ using the max operation.

Figure 13: Total acoustic energy penetrating into the solder bump between Models A and B at four transducer positions.